Phase field modeling of cracks in ice

Rabea Sondershaus and Ralf Müller and Dietmar Gross and Angelika Humbert

Abstract

Calving of iceberg at ice shelves and floating glacier tongues is a poorly understood process, hence a physically motivated calving law is not yet existing. The demands on developing appropriate models for calving is large, as calving rates are needed for large scale ice sheet models that simulate the evolution of ice sheets. Here, we present a new approach for simulating fracture in ice. Our model is based on a finite strain theory for a viscoelastic Maxwell material, as the large simulation time leads to high strains. The fracturing process is simulated using a fracture phase field model that takes into account the elastic strain energy. We conduct simulations for a typical calving front geometry, with ice rises governing the formation of cracks. To represent the stress state adequately, we first conduct a spin-up to allow the viscous contribution to develop before the fracture phase field is computed. The analysis comprises the assessment of the crack path in comparison to observations, the influence of the spin-up, as well as elastic versus viscous strain contributions based on Hencky strain. Additionally, an estimate of released energy based on high resolution optical imagery of a Greenlandic calving front is presented.

Rabea Sondershaus
Institute for Mechanics, Technical University of Darmstadt, Darmstadt, Germany e-mail: rabea.sondershaus@tu-darmstadt.de

Ralf Müller
Institute for Mechanics, Technical University of Darmstadt, Darmstadt, Germany e-mail: ralf.mueller@mechanik.tu-darmstadt.de

Dietmar Gross
Institute for Mechanics, Technical University of Darmstadt, Darmstadt, Germany e-mail: gross@mechanik.tu-darmstadt.de

Angelika Humbert
Alfred-Wegener-Institut Helmholtz Zentrum für Polar- und Meeresforschung, Bremerhaven, Germany and Department of Geoscience, University of Bremen, Bremen e-mail: angelika.humbert@awi.de

1 Introduction

Ice at stresses and strain-rates typically occurring in ice sheets and ice shelves shows a dominant brittle behaviour [1]. The fracture toughness of polycrystalline ice was found in laboratory experiments to be $K_{Ic} = 95.35 \pm 16.69 \text{kPa m}^{1/2}$ [2]. Cracks in ice are evolving episodically. The length of such cracks is often on the order of kilometers. They either intersect the ice in vertical (thickness) direction entirely (so called rifts) when they propagate in horizontal direction, or they open up in vertical direction (crevasses) with crack face distance in the order to 1-10's meters. At calving fronts, crack propagation is eventually leading to the detachment of icebergs. This is a normal process of mass loss of floating ice masses. In contrast, ice shelf break-up events or the disintegration of floating tongues represent instability of ice masses. Understanding of fracture formation and evolution is thus of major importance for projecting the future of ice sheets. Yet physically based calving laws are not existing. In Fig. 1 the calving front situation at Greenland's largest floating ice tongue called Nioghalvfjerdsbræ is shown. The glacier tongue is grounded at several points which are called ice rises and are marked in blue. At these points cracks emerge in the ice shelf, as can be seen in the satellite imagery, Fig. 1b).

Glacial ice was found to be a viscolelastic fluid following a Maxwell rheology [3, 4, 5]. The elastic behavior is assumed to be compressible, as it is common for crystalline materials, while the viscous flow behavior originates from incompressible inelastic processes. The viscosity is strongly influenced by the temperature which varies in ice sheets primarily in vertical direction (cold at the top, warm at the base)

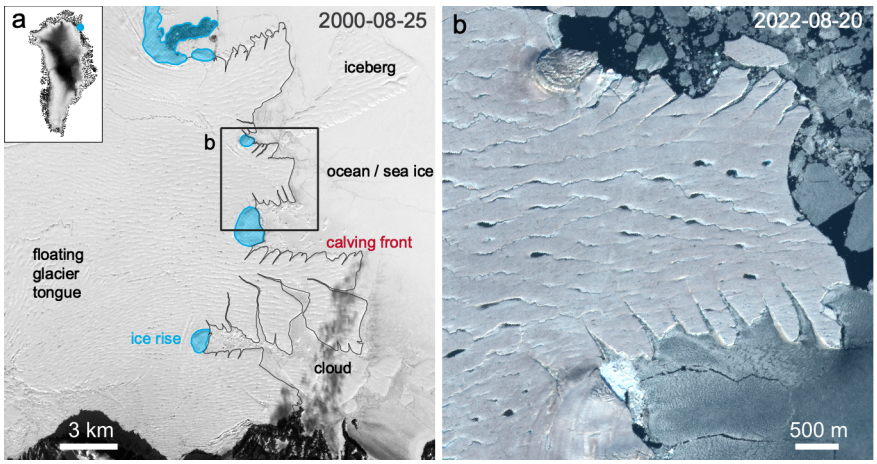

Fig. 1 Overview of a typical calving front situation. The left panel shows a Landsat-7 satellite image of the calving front (black line) of Nioghalvfjerdsbræ, Greenland's largest floating ice tongue. The blue areas are ice rises. The right panel (Sentinel-2 imagery) is a zoom into a part of the ice front (box in the left panel) where cracks around the ice rises and along the lateral margins of the ice are visible.

and in flow direction (cold in the high elevated interior of the ice sheet, warmer at the lower ice sheet margins). In general, ice sheets and ice shelves are hot materials, as their homologous temperature is extremely high. Its characteristic time ranges from 30 days for $\eta = 10^{15}$Pa s to 8.4 years for $\eta = 10^{17}$Pa s assuming a Young's modulus of 1 GPa and $\nu = 0.325$ This exemplifies that long computation times are needed to solve the problems adequately and as a consequence, a non-linear strain theory is required. For glacial ice a finite strain theory for a Maxwell rheology was first formulated by [6] and applied to a realistic ice shelf geometry in [7].

In the present investigation a fracture phase field model is proposed to describe the failure of ice due to crack formation and propagation. The general concept of phase field models is the representation of a sharp interface, such as for example crack surfaces or grain boundaries by means of a continuous scalar field $s(x,t)$. The order parameter s represents the 'phase' e.g. the state of the material, where for fracture the intact material is specified by $s = 1$ and the fractured material by $s = 0$. The transition between these states is smoothed out leading to a diffuse representation of the crack.

The benefit of the diffuse representation is the prevention of costly remeshing during crack growth. Furthermore, the fracture phase field method is capable to simulate crack propagation as well as crack initiation and crack branching. In the last decade, the phase field method has become well established for fracture simulations and was used for a variety of fracture processes such as brittle [8, 9, 10], dynamic [11, 12, 13], fatigue [14, 15, 16] and hydraulic fracture [17, 18]. Moreover different material behaviours for instance anisotropy [19, 20, 21], plasticity [22, 23, 24] and viscoelasticity [25, 26, 27] were studied. In this contribution, we will focus on the latter by combining the phase field model with a viscoelastic material description to capture the long and short term deformation of ice adequately. Since large time scales are considered in this study, the theory of small strains is no longer sufficient and the framework of finite deformations is needed.

The first application of phase field modelling for fracture in ice was presented by [28], with a focus on hydrofracture. This study assumed a linear elastic material response of the glacier, disregarding any viscous deformation, and a 2D glacier geometry. [29] presented a stress-based phase field fracture formulation, which was used to simulate hydrofracture in 2D and 3D including a viscous rheology. Crack initiation at ice rises was studied in [30] based on a viscoelastic phase field formulation for Maxwell materials. All above mentioned studies were assuming linear strain.

This text is organised as follows: First, the visocelastic material model at finite strains is introduced before explaining the phase field for fracture. Subsequently, we present the numerical aspects of the implementation and the simulation concept. Section 3 is focusing on the simulation results. In a last part the energy release from observations is estimated.

2 Theory

2.1 Non-linear strain theory for viscoelastic material

The viscoelastic behaviour of ice can be described by the rheological Maxwell model, where an elastic element is in series with a viscous element. The basics of such a viscoelastic material description are briefly outlaid in the following.

In a finite strain formulation of a viscoelastic material a distinction between a (stress-free) reference configuration κ_r and a current configuration κ_t at time t is made. Both configurations as well as their corresponding quantities are sketched in Fig. 2. A central quantity in the description of the kinematics is the deformation gradient $\mathbf{F}$, defined as

$$\mathbf{F}(\mathbf{X}, t) = \frac{\partial \mathbf{x}}{\partial \mathbf{X}} = \mathbf{1} + \frac{\partial \mathbf{u}}{\partial \mathbf{X}}. \tag{1}$$

It is noted that $\mathbf{x}$ describes the position of a material point in the current configuration, whereas $\mathbf{X}$ describes the position of the same material point in the reference configuration. The vector $\mathbf{u} = \mathbf{x} - \mathbf{X}$ is referred to as displacement vector. As the deformation gradient also contains rigid body motion, it is not a useful measure for strain. To this end the Green-Lagrange strain tensor $\mathbf{E}$ is introduced

$$\mathbf{E} = \frac{1}{2}(\mathbf{C} - \mathbf{1}) \tag{2}$$

with the right Cauchy-Green tensor $\mathbf{C}$

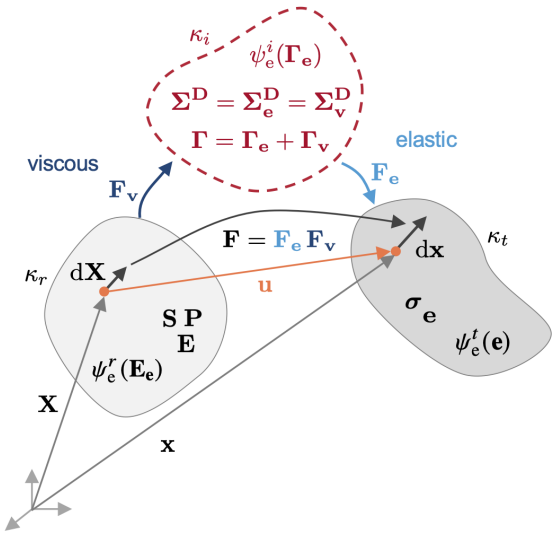

Fig. 2 Kinematics of the problem in the reference κ_r (light grey) and current configuration κ_t (dark grey). For viscoelastic materials the intermediate configuration κ_i (red dashed line) is the configuration in which the constitutive relation is derived.

$$\mathbf{C} = \mathbf{F}^{\mathbf{T}}\mathbf{F} \tag{3}$$

as a strain measure in the reference configuration κ_r. Its counterpart in the current configuration κ_t is the Euler-Almansi strain tensor $\mathbf{e}$

$$\mathbf{e} = \frac{1}{2}(\mathbf{1} - \mathbf{b}^{-1}) \tag{4}$$

that contains the left Cauchy-Green tensor $\mathbf{b}$

$$\mathbf{b} = \mathbf{F}\mathbf{F}^{\mathbf{T}}. \tag{5}$$

The kinematic equations are complemented by balance laws. To describe the motion of an ice sheet/ice shelf the balance of linear momentum is considered. As the focus is on horizontal plane of the extent of the ice sheet/ice shelf/glacier gravitational forces vanish. Furthermore, neglecting inertia terms the balance of linear momentum reduces to the equilibrium condition, given by

$$\mathrm{Div}\,\mathbf{P} = 0 \tag{6}$$

with the divergence in κ_r being denoted with $\mathrm{Div}(\cdot)$ and $\mathbf{P}$ the first Piola-Kirchhoff tensor, as a stress tensor referring to the reference configuration. The transformation between $\mathbf{P}$ and the Cauchy stress tensor $\boldsymbol{\sigma}$ in the current configuration κ_t is given by

$$\mathbf{P}\mathbf{N}\,\mathrm{d}A = \sigma\mathbf{n}\,\mathrm{d}a \tag{7}$$

with $\mathbf{N}, \mathbf{n}$ the normal vectors and $\mathrm{d}A, \mathrm{d}a$ the infinitesimal area elements in the reference κ_r and current configuration κ_t, respectively. Infinitesimal area elements transform according to Nanson's formula

$$J\mathbf{F}^{-\mathbf{T}}\mathbf{N}\,\mathrm{d}A = \mathbf{n}\,\mathrm{d}a \tag{8}$$

with $J = \det(\mathbf{F})$.

To take the viscous part into account the intermediate configuration k_i (see Fig. 2) is introduced. The key concept for modelling finite viscoelasticity is the multiplicative decomposition of the deformation gradient into an elastic $\mathbf{F_e}$ and viscous $\mathbf{F_v}$ part

$$\mathbf{F} = \mathbf{F_e}\mathbf{F_v}, \tag{9}$$

which was introduced by [31] in the context of finite plasticity and first applied to ice deformation by [6]. As a consequence, the strain tensor $\boldsymbol{\Gamma}$ in the intermediate configuration is also decomposed into an elastic $\boldsymbol{\Gamma}_\mathbf{e}$ and a viscous $\boldsymbol{\Gamma}_\mathbf{v}$ part, but the decomposition is, comparable to the Maxwell model for small strains, additive

$$\begin{aligned}\boldsymbol{\Gamma} &= \mathbf{F_v}^{-\mathrm{T}}\mathbf{E}\mathbf{F_v}^{-1} = \frac{1}{2}\mathbf{F_v}^{-\mathrm{T}}(\mathbf{F}^{\mathbf{T}}\mathbf{F} - \mathbf{1})\mathbf{F_v}^{-1} \\ &= \frac{1}{2}(\mathbf{F_e}^{\mathrm{T}}\mathbf{F_e} - \mathbf{F_v}^{-\mathrm{T}}\mathbf{F_v}^{-1}) = \boldsymbol{\Gamma}_\mathbf{e} + \boldsymbol{\Gamma}_\mathbf{v}.\end{aligned} \tag{10}$$

Accordingly the elastic strain is given by

$$\boldsymbol{\Gamma}_\mathbf{e} = (1/2)(\mathbf{F_e}^{\mathrm{T}}\mathbf{F_e} - \mathbf{1}) \tag{11}$$

and the viscous strain in the intermediate configuration is obtained by

$$\boldsymbol{\Gamma}_\mathbf{v} = (1/2)(\mathbf{1} - \mathbf{F_v}^{-\mathrm{T}}\mathbf{F_v}^{-1}). \tag{12}$$

It is important to note that the additive decomposition of the strain is only viable in the intermediate configuration [1].

The introduction of an intermediate configuration can be seen as a constitutive assumption. The stress tensor in intermediate configuration $\boldsymbol{\Sigma}$ depends on the elastic strain $\boldsymbol{\Gamma}_\mathbf{e}$ as $\boldsymbol{\Sigma} = f(\boldsymbol{\Gamma}_\mathbf{e})$, which for an isotropic material is given by

$$\boldsymbol{\Sigma} = \lambda\,\mathrm{tr}(\boldsymbol{\Gamma}_\mathbf{e})\mathbf{1} + 2\mu\boldsymbol{\Gamma}_\mathbf{e} \tag{13}$$

with the Lamé constants λ and μ. This form of material law is known as St. Venant-Kirchhoff material. Eq. 13 can be reformulated easily to

$$\boldsymbol{\Sigma} = \lambda\,\mathrm{tr}(\boldsymbol{\Gamma} - \boldsymbol{\Gamma}_\mathbf{v})\mathbf{1} + 2\mu(\boldsymbol{\Gamma} - \boldsymbol{\Gamma}_\mathbf{v}) \tag{14}$$

with the viscous strain in the intermediate configuration $\boldsymbol{\Gamma}_\mathbf{v}$.

Similar to the additive composition of the strain in κ_i, the strain-rates are decomposed. Dealing with finite strains, objective time derivatives are needed. To this end, the lower Oldroyd rate is chosen.

$$\overset{\triangle}{\boldsymbol{\Gamma}}_\mathrm{e} = \dot{\boldsymbol{\Gamma}}_\mathbf{e} + \mathbf{l}_\mathbf{v}^{\mathbf{T}}\boldsymbol{\Gamma}_\mathbf{e} + \boldsymbol{\Gamma}_\mathbf{e}\mathbf{l}_\mathbf{v} \tag{15}$$

is the elastic strain-rate, while

$$\overset{\triangle}{\boldsymbol{\Gamma}}_\mathrm{v} = \dot{\boldsymbol{\Gamma}}_\mathbf{v} + \mathbf{l}_\mathbf{v}^{\mathbf{T}}\boldsymbol{\Gamma}_\mathbf{v} + \boldsymbol{\Gamma}_\mathbf{v}\mathbf{l}_\mathbf{v} \tag{16}$$

is the viscous strain-rate in κ_i. The viscous deformation gradient $\mathbf{l}_\mathbf{v}$ is computed from

$$\mathbf{l}_\mathbf{v} = \dot{\mathbf{F}}_\mathrm{v}\mathbf{F}_\mathbf{v}^{-\mathbf{1}}. \tag{17}$$

The transformation (push forward operation) of the Green-Lagrange strain tensor into the intermediate configuration then reads

[1] Later on, we will introduce a strain measure that allows to compute the elastic and viscous strain components in the reference configuration.

$$\overset{\triangle}{\boldsymbol{\Gamma}} = \mathbf{F_v}^{-\mathrm{T}}\dot{\mathbf{E}}\mathbf{F_v^{-1}} = \mathbf{F_v}^{-\mathrm{T}}\left(\overline{\mathbf{F_v^T}\boldsymbol{\Gamma}\mathbf{F_v}}\right)\mathbf{F_v^{-1}} = \dot{\boldsymbol{\Gamma}} + \mathbf{l_v^T}\boldsymbol{\Gamma} + \boldsymbol{\Gamma}\,\mathbf{l_v}. \tag{18}$$

To complete the viscoelastic constitutive model we need to define the stress in conjunction with an evolution law of the viscous strain, described by the viscous right Cauchy-Green tensor

$$\mathbf{C_v} = \mathbf{F_v^T}\mathbf{F_v}. \tag{19}$$

We define a strain tensor in κ_r as the difference between total and viscous strains as

$$\mathbf{E_e} = \frac{1}{2}\left(\mathbf{C} - \mathbf{C_v}\right) \tag{20}$$

Setting the (deviatoric) elastic and viscous stresses equal

$$2\eta\overset{\triangle}{\boldsymbol{\Gamma}}_{\mathrm{v}} = 2\mu\left(\boldsymbol{\Gamma} - \boldsymbol{\Gamma_v} - \frac{1}{3}\mathrm{tr}(\boldsymbol{\Gamma} - \boldsymbol{\Gamma_v})\mathbf{1}\right) = 2\mu\boldsymbol{\Gamma}_\mathbf{e}^\mathbf{D}, \tag{21}$$

the evolution equation of the viscous part $\overset{\triangle}{\boldsymbol{\Gamma}}_{\mathrm{v}}$ of the viscous strain tensor in the intermediate configuration is obtained as a function of the total strain difference $\boldsymbol{\Gamma} - \boldsymbol{\Gamma_v}$. Note that in the above equation the deviatoric part of $\boldsymbol{\Gamma} - \boldsymbol{\Gamma_v} = \boldsymbol{\Gamma_e}$ is used. This establishes an isochoric viscous deformation. The evolution law can also be expressed in terms of the right Cauchy-Green tensor $\mathbf{C_v}$, resulting in

$$\eta\dot{\mathbf{C}}_\mathbf{v} = \mu\left(\mathbf{C} - \frac{1}{3}\mathrm{tr}(\mathbf{C}\mathbf{C_v^{-1}})\mathbf{C_v}\right). \tag{22}$$

Details are omitted here for the sake of compactness, but can be found in [6, 32]. Finally for the implementation the second Piola-Kirchhoff stress tensor is needed. It can be computed by a pull back of the stress $\boldsymbol{\Sigma}$ from the intermediate configuration κ_i on the reference configuration κ_r with the help of the viscous part of the deformation gradient $\mathbf{F_v}$

$$\begin{aligned}\mathbf{S} &= \mathbf{F_v^{-1}}\,\boldsymbol{\Sigma}\,\mathbf{F_v^{-T}} \\ &= \frac{\lambda + (2/3)\mu}{2}\left[\mathrm{tr}(\mathbf{C}\mathbf{C_v^{-1}}) - 3\right]\mathbf{C_v^{-1}} + \mu\left[\mathbf{C_v^{-1}}\mathbf{C}\mathbf{C_v^{-1}} - \frac{1}{3}\mathrm{tr}(\mathbf{C}\mathbf{C_v^{-1}})\mathbf{C_v^{-1}}\right].\end{aligned} \tag{23}$$

As the viscous deformation is isochoric the $J_v = \det(\mathbf{F})$ does not appear in the above pull back operation.

The above derivations are formulated for the general 3D case. The adjustments for e.g. the computation of deviatoric tensor components in 2D have to be made, accordingly.

In the formulation of the fracture mechanical model the elastic energy density is needed. The elastic energy density of an isotropic St. Venant-Kirchhoff material in κ_i is given by

$$\psi_{\mathrm{e}}^{i}(\mathbf{\Gamma_e}) = \frac{1}{2}\mathbf{\Gamma_e} : \mathbb{C}\mathbf{\Gamma_e} = \frac{\lambda}{2}\mathrm{tr}(\mathbf{\Gamma_e})^2 + \mu\mathbf{\Gamma_e} : \mathbf{\Gamma_e} \tag{24}$$

with $\mathbb{C}$ the elasticity tensor defined by the Lamé constants λ, μ [33]. The elastic energy density of a St. Venant-Kirchhoff material in κ_r is given by

$$\psi_{\mathrm{e}}^{r}(\mathbf{E_e}) = \frac{1}{2}\mathbf{E_e} : \mathbb{C}\mathbf{E_e} = \frac{\lambda}{2}\mathrm{tr}(\mathbf{E_e})^2 + \mu\mathbf{E_e} : \mathbf{E_e} \tag{25}$$

as $J_v = 1$ due to $dV = dV^i$.
Finally, the elastic energy density of a St. Venant-Kirchhoff material in κ_t is given by

$$\psi_{\mathrm{e}}^{t}(\mathbf{e}) = \frac{1}{2}\mathbf{e_e} : \mathbb{C}\mathbf{e_e} = \frac{\lambda}{2}\mathrm{tr}(\mathbf{e_e})^2 + \mu \tag{26}$$

.
In order to evaluate the elastic and viscous components of strain, we introdue a logarithmic strain measure, the Hencky strain [34] that reads

$$\boldsymbol{\varepsilon}^{\mathbf{H}} = \frac{1}{2}\ln\left(\mathbf{F}^{\mathbf{T}}\mathbf{F}\right) = \frac{1}{2}\ln(\mathbf{C}) \tag{27}$$

and an additive decomposition of the Hencky strain as

$$\boldsymbol{\varepsilon}_{\mathbf{e}}^{\mathbf{H}} = \boldsymbol{\varepsilon}^{\mathbf{H}} - \boldsymbol{\varepsilon}_{\mathbf{v}}^{\mathbf{H}} = \frac{1}{2}\ln(\mathbf{C}) - \frac{1}{2}\ln(\mathbf{C_v}) \tag{28}$$

With this the formulation of the finite strain theory for a viscoelastic Maxwell material is complete. Next, we introduce the fracture phase field model for viscoelastic materials under finite strains.

2.2 The phase field model of fracture

The general idea of the phase field method of fracture is based on Griffith's theory of fracture, in which failure occurs once a material specific critical value of the energy release rate $\mathcal{G}_c$ is reached. It is a material parameter that is related to the fracture toughness $\mathrm{K_{Ic}}$ by $\mathcal{G}_c = {\mathrm{K_{Ic}}}^2(1-\nu^2)/\mathrm{E}$ in the plane strain case. The energy available for crack formation is given by the strain energy. Hence the energy potential Π of a body Ω with a sharp crack interface Γ_f reads

$$\Pi = \int_{\Omega\setminus\Gamma_\mathrm{f}} \psi_\mathrm{e}\, dV + \int_{\Gamma_\mathrm{f}} \psi_\mathrm{f}\, dA - \int_{\partial\Omega} \mathbf{t}_0 \cdot \mathbf{u}\, dA \tag{29}$$

with the first term describing the strain energy and the second term the energy required for fracture along the crack. The last term represents the traction boundary condition with a traction in the reference configuration $\mathbf{t}_0 = \mathbf{PN}$ and $\mathbf{u}$ the displacement. As mentioned above the sharp crack interface is smoothed out over a length

scale l_0 as sketched in Fig. 3. The phase field method is hence approximating the energy for fracture as a volume integral over the critical energy release rate $\mathcal{G}_c$ multiplied by the crack surface (density) A_{l_0}

$$\int_\Omega \psi_f dV = \int_\Omega \mathcal{G}_c \, A_{l_0} dV \approx \int_{\Gamma_f} \mathcal{G}_c \, dA \ . \tag{30}$$

The crack surface density depends on the length scale l_0 which describes the transition width between intact and broken material as well as on the order parameter s. We use the Ambrosio and Tortorelli approximation [35] which is given by

$$\int_\Omega \mathcal{G}_c \, A_{l_0} dV = \int_\Omega \mathcal{G}_c \left(\frac{(1-s)^2}{4l_0} + l_0 \nabla s \cdot \nabla s \right) dV \tag{31}$$

including a local part $(1-s)^2/4l_0$ and a non-local contribution $l_0 \nabla s \cdot \nabla s$ of the crack surface density. It satisfies the Γ-convergence criterion and converges for $l_0 \to 0$ to a sharp crack in case of a brittle material [36, 37].
With increasing damage due to crack formation and propagation, the material stiffness is reduced. This is introduced by a degradation function $g(s)$ given as a quadratic function $g(s) = s^2 + \eta_{RS}$ in which $\eta_{RS} \ll 1$ is a residual stiffness that ensures for an entirely broken material a numerically well conditioned system. For a vanishing residual stiffness η_{RS} the degradation function satisfies $g(s = 1) = 1$ as well as

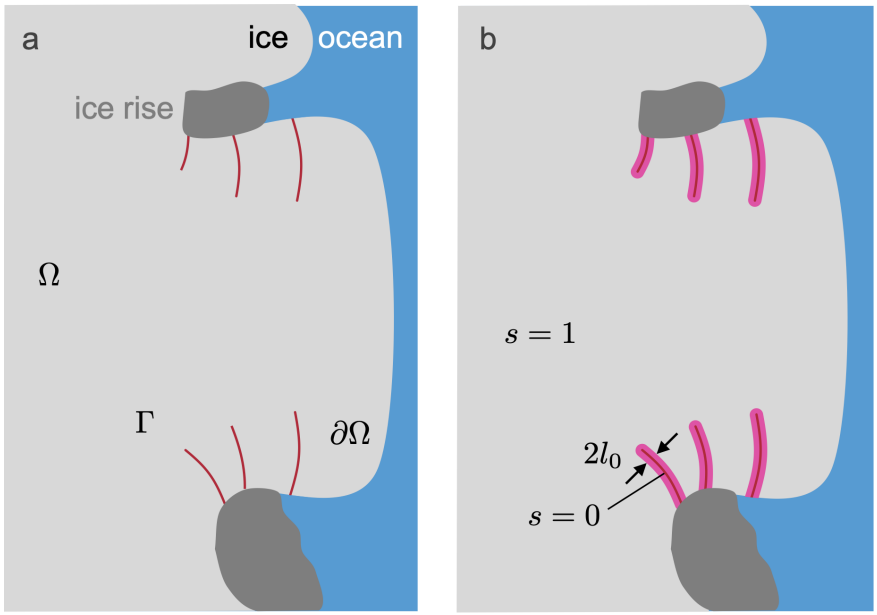

Fig. 3 Sketch of the concept of phase field modelling of fracture. The left panel resembles sharp cracks, while the right panel highlights smeared out cracks represented by a continuous phase field.

$g(\mathrm{s}=0)=0$ and

$$\frac{\partial g}{\partial \mathrm{s}} \leq 0\,, \quad \frac{\partial g}{\partial \mathrm{s}}\,|_{\mathrm{s}=0} = 0. \tag{32}$$

To ensure irreversibility of the crack, the phase field is set to 0 once it has reached a critical value.
The regularised energy potential including the work of the surface tractions becomes

$$\Pi_r = \int_\Omega g(\mathrm{s})\psi_\mathrm{e}\, dV + \int_\Omega \psi_\mathrm{f}\, dV - \int_{\partial\Omega} \mathbf{t}_0 \cdot \mathbf{u}\, dA\,. \tag{33}$$

Next ψ_e is specified. Assuming a St. Venant-Kirchhoff material that was already introduced above, the elastic strain energy is split into a volumetric and a deviatoric part

$$\psi_\mathrm{e} = \frac{\lambda}{2}\mathrm{tr}(\mathbf{E_e})^2 + \mu\mathbf{E_e} : \mathbf{E_e} = \frac{1}{2}K\mathrm{tr}(\mathbf{E_e})^2 + \mu\mathbf{E_e^D} : \mathbf{E_e^D} \tag{34}$$

with the bulk modulus $K = \lambda + \frac{2}{3}\mu$.
Crack evolution is assumed to occur under tension only, thus the volumetric strain energy density is split into a positive and a negative part. To this end the (signed) Macaulay brackets are defined as

$$\langle \mathrm{x}\rangle_+ = \begin{cases} \mathrm{x} & \text{for } \mathrm{x} \geq 0 \\ 0 & \text{for } \mathrm{x} < 0 \end{cases} \qquad \langle \mathrm{x}\rangle_- = \begin{cases} \mathrm{x} & \text{for } \mathrm{x} \leq 0 \\ 0 & \text{for } \mathrm{x} > 0 \end{cases} \tag{35}$$

and are applied to the elastic volumetric strain $\mathrm{tr}(\mathbf{E_e})$.
Incorporating all the above features the final version of the phase field potential is given by

$$\begin{aligned} \Pi_\mathrm{r} = &\int_\Omega g(\mathrm{s}) \left(\frac{1}{2}K\langle \mathrm{tr}(\mathbf{E_e})\rangle_+^2 + \mu\mathbf{E_e^D} : \mathbf{E_e^D} \right) dV + \int_\Omega \frac{1}{2}K\langle \mathrm{tr}(\mathbf{E_e})\rangle_-^2\, dV \\ &+ \int_\Omega \mathcal{G}_\mathrm{c} \left(\frac{(1-\mathrm{s})^2}{4\mathrm{l}_0} + \mathrm{l}_0 \nabla \mathrm{s} \cdot \nabla \mathrm{s} \right) dV - \int_{\partial\Omega} \mathbf{t}_0 \cdot \mathbf{u}\, dA\,. \end{aligned} \tag{36}$$

In the approach presented here, we only consider an elastic component to the strain energy, disregarding a direct influence of the viscous component. In this way we model elastic crack evolution in a viscoelastic material.
In order to solve the problem, Eq. 36 is minimized with respect to the displacement field $\mathbf{u}$ by setting the variation with respect to $\mathbf{u}$ to zero: $\delta_\mathrm{u}\Pi = 0$. This renders the equilibrium conditions and the traction boundary conditions. To obtain an evolution equation for the phase field a time dependent Ginzburg-Landau equation is used to relate the change of the fracture field s to the variational derivative of the phase field potential with respect to s

$$\dot{\mathrm{s}} = -\mathrm{M}\delta_\mathrm{s}\Pi_\mathrm{r} \tag{37}$$

with M the mobility constant. The mobility constant M is introduced to ensure numerical stability and acts as a rate dependent regularization in situations with

Table 1 Model parameters

parameter	value	unit
η	$5 \cdot 10^{14}$	Pa s
E	1	GPa
ν	0.325	
$\mathcal{G}_c$ (for an ice thickness of 100 m)	901	$\mathrm{J\,m^{-2}}$
l_0	198	m
M	10^5	
η_{RS}	0.001	

rapid crack evolution, such as crack initiation.

2.3 Numerics

The model was implemented in the finite element framework FEniCS [38], more specifically we implemented Eq. (36) and used the automatic derivative to obtain the variations with respect to the displacement $\mathbf{u}$ and the phase field variable s. Setting the variation with regard to $\mathbf{u}$ to zero renders the equilibrium condition. The variation with respect to s provides the driving force, c.f. Eq. (37), where we have chosen a mobility constant of $M = 10^5$. The rate of s in Eq. (37) is integrated in time using a backward Euler scheme. The residual stiffness η_{RS} in the degradation function has been chosen to be 0.001 and s is fixed to zero for all further time steps if $s \leq 0.05$. All model parameters used throughout the simulations can be found in Tab. 1. To solve the system of equations, a monolithic scheme is used and thus the displacement field $\mathbf{u}$ and the fracture field s are calculated simultaneously. The internal variable $\mathbf{C_v}$ is obtained from the evolution Eq. (38) where an forward Euler scheme is used to approximate the rate $\dot{\mathbf{C}}_\mathbf{v}$

$$\dot{\mathbf{C}}_\mathbf{v} = \frac{\mathbf{C_v}^{n+1} - \mathbf{C_v}^{n}}{\Delta t} \tag{38}$$

resulting in an equation for the $\mathbf{C_v}$ at time step $n + 1$:

$$\mathbf{C_v}^{n+1} = \frac{\mu}{\eta}\Delta t \left(\mathbf{C}^n - \frac{1}{3}\mathrm{tr}\left(\mathbf{C}^n (\mathbf{C_v}^n)^{-1} \right) \right) + \mathbf{C_v}^n \,. \tag{39}$$

The displacement field $\mathbf{u}$ and the fracture field s are interpolated linearly using triangular elements. The internal variable $\mathbf{C_v}$ is constant in each element. Due to the non-linear coupling of $\mathbf{u}$ and s a Newton-Raphson scheme is applied to obtain the values at a new time step t_{n+1} form the previous time step at t_n. The embedded linear system is solved using the solver MUMPS [39]. Especially in cases with rapid crack evolution, the Newton-Raphson scheme may not converge (relative and absolute tolerance). Thus, in cases where the Newton-Raphson scheme does not converge

in 15 iterations the time step is halved. If the Newton-Raphson scheme converges less than 5 iterations the time step is doubled. This heuristic time step adjustment improves the numerical stability and guarantees a certain efficiency.

2.4 Scenarios, setup and spin-ups

Different geometries are considered here, which are motivated by the typical calving front situations as shown in the right panel of Fig. 1. At first (Case 1) a square ice shelf area is used with inflow from left and a calving front on the right side as shown in Fig. 4. Upper and lower boundaries are assumed to be ice shelf internal boundaries. To mimic this situation vertical displacements are blocked while the horizontal motion is not constrained. The ice rises are modelled as holes, with a homogeneous Dirichlet boundary condition $\mathbf{u} = \mathbf{0}$. At the inflow boundary the displacement is also set to zero, whereas at the outflow a constant velocity of 0.2 m/day in horizontal direction is applied, leading to an overall tension of the domain. This setup resembles the situation at an ice shelf that is increasing in velocity towards the ice front.

In Case 2 a free floating ice tongue is anticipated. Thus from the inflow to the ice rise identical boundary conditions as in Case 1 are used. The ice rise are again modelled as fully attached ice by setting $\mathbf{u} = \mathbf{0}$ along both quarter-circles. As in the first example the lateral margins upstream of the ice rises are internal boundaries, where the vertical displacements are set to zero. The lateral boundary conditions of the ice tongue are traction free. The calving front is again loaded by a linearly in time increasing displacement load of 0.2 m/day. Both meshes were created in Gmsh [40] and have been refined towards the circles or quarter circles representing the ice rises.

In many engineering applications a load is applied to an initially unloaded body. The task is to simulate changes in stress, strain and associated crack formation during the application of a time dependent load. In the case under consideration

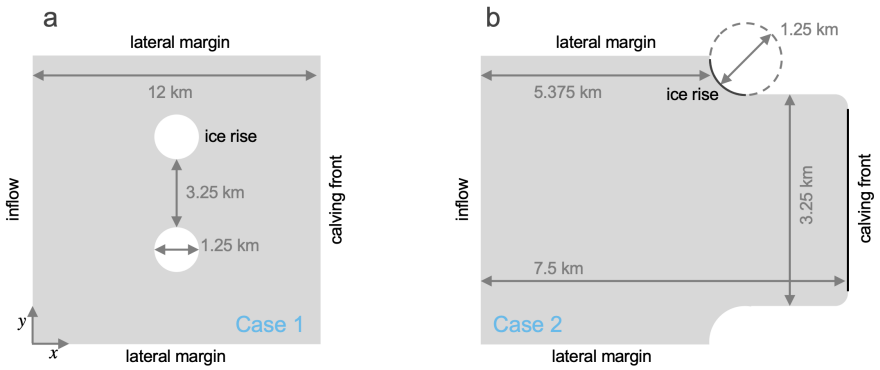

Fig. 4 Geometry setup of the numerical experiments, circles resemble ice rises.

here, a natural system is analysed that has undergone a long load and deformation history. Therefore, the viscous strain field is already well developed, while the elastic component is becoming more important in the vicinity of the calving front. This becomes more evident when considering the characteristic time again, as the viscous component only evolved over larger time scales of month to years. To capture this in this contribution, so called spin-up simulations were performed. In the spin-up the fracture phase field model is switched off, but the viscoelastic deformation is allowed to develop. As an order of magnitude for the time scale, the time span between the fracture formation of the lateral cracks visible in Fig. 1 is considered, which is about one year. As the fracture phase field is not solved for, only slow viscoelastic processes occur and the time steps in the spin-up runs can be larger, but due to the explicit time scheme a maximum time step of a day is allowed. After the completion of the spin-up runs, the displacement $\mathbf{u}$ and viscous strain field $\mathbf{C_v}$ are used as the initial state for subsequent fracture phase field simulations.

3 Results

3.1 Crack evolution and strain for ice rises within the ice shelf

We present the fracture phase field of Case 1 in Fig. 5 for different initial conditions. We investigate the case of no spin-up and several spin-up simulations with different time periods varying between 10 up to 40 weeks. The crack paths differ in all experiments. In all cases the crack evolution starts at the downstream (lee) side of ice rises and then propagates along the circles until it deviates from the ice rise margin and cracks in the area between the ice rises are formed. Once the cracks are unified the fracture evolves towards the boundaries of the domain. For the experiment without spin-up the crack path is a nearly straight line between the ice rises and the lateral margins of the ice body. The crack paths for experiments with spin-up runs differ strongly from the experiment without spin-up. With shorter spin-up times, thus less viscous deformation, the crack path is more branched then with longer spin-up times. More than one crack forms at the ice rises. All cases with spin-up lead to a final crack path between the ice rises of a bow-like shape. Also between the ice rises and the lateral margins, the crack path is more inclined as compared to the experiment without spin-up. In the downstream part of the ice body, the phase field is also reduced for all pre-deformed cases, while the phase field without spin-up remains fully intact in almost all areas around except the main crack. While conducting the simulations, we observe that the transition between spin-up to the full problem including the fracture phase field is prone to numerical difficulties. The time step is becoming very small, as the spreading of the crack is very quick. This behaviour is referred to as model shock in the following.

In order to quantitatively capture the influence of elastic and viscous strain we resort to the additive decomposition of the Hencky strains as introduced in (28). For this purpose, Fig. 6 presents the ratio $\boldsymbol{\varepsilon}_\mathbf{e}^\mathbf{H}/(|\boldsymbol{\varepsilon}_\mathbf{e}^\mathbf{H}| + |\boldsymbol{\varepsilon}_\mathbf{v}^\mathbf{H}|)$ and $\boldsymbol{\varepsilon}_\mathbf{v}^\mathbf{H}/(|\boldsymbol{\varepsilon}_\mathbf{e}^\mathbf{H}| + |\boldsymbol{\varepsilon}_\mathbf{v}^\mathbf{H}|)$ for

selected experiments: (a) no spin-up, (b) with 15 weeks spin-up and (c) with 40 weeks of pre-loading. The Hencky strains are shown at the same time as the phase field s in Fig. 5 It can be observed that elastic strains occur primarily as an instantaneous reaction to crack propagation and are thus very large in the area of the crack and at the crack tip. It is worth to note that this concentration of the elastic strains occurs more pronounced in the simulations with spin-up. This is an indication of the model shock. The system can only account for the stress redistribution by elastic responses. In the situation with no spin-up, elastic strain forms a compression arc to support the applied external load. In the simulations without spin up, the crack is almost invisible in the strain distributions, elastic or viscous, see Fig. 6a,b. In situations with spin-up the viscous strain contribution vanishes in the crack region, see Fig. 6 d,f. This is due to the longer viscous time scale, indication again the feature referred to as model shock.

To better understand the temporal evolution of the fracture process, Fig. 7 reports the fracture phase field and the elastic Hencky strain contribution for a spin-up of 10 weeks. The system is so highly stressed that not only one, but three cracks from at each ice rise (hole), see Fig. 7c. The two cracks towards the middle of the domain converge into one crack at each ice rise which afterwards grows further into the area between the ice rises. The two cracks this middle area unify and form a large crack that connects the two ice rises. Later the lateral cracks grow towards the boundaries resulting in a final splitting of the ice block. Again the different time scales of the crack propagation and the viscous flow are worth mentioning. Compared to the 'slow' flow process the crack propagates almost instantaneously. There is again a strong correlation between the elastic strain distribution and the crack path. To support this statement the arc-like tensile elastic strain distribution in Fig. 7d is mentioned. Later, see Fig. 7f, the crack path follows this arc-like distribution. In regions with compressive elastic strain, such as the upstream boundary of the ice rise, cracks are suppressed.

3.2 Crack evolution and strain for floating tongue

Here we present the results of a more realistic calving front geometry (see also Fig. 1). The evolution of the phase field is displayed in Fig. 8 for four instances in time without a spin-up run. The cracks emerge downstream of the ice rises and grow from the transition between ice rise and calving front in lateral direction. In the early stages of crack propagation the direction is more or less straight, while the crack path is slightly diverted as the cracks get closer to each other. The final stage is a slight bow form. The crack width grows wide at the calving front. In contrast to the case in which the ice rises are situated in the center of the ice body, the phase field downstream the crack is not impacted, as the ice does not have to detach form the ice rise.

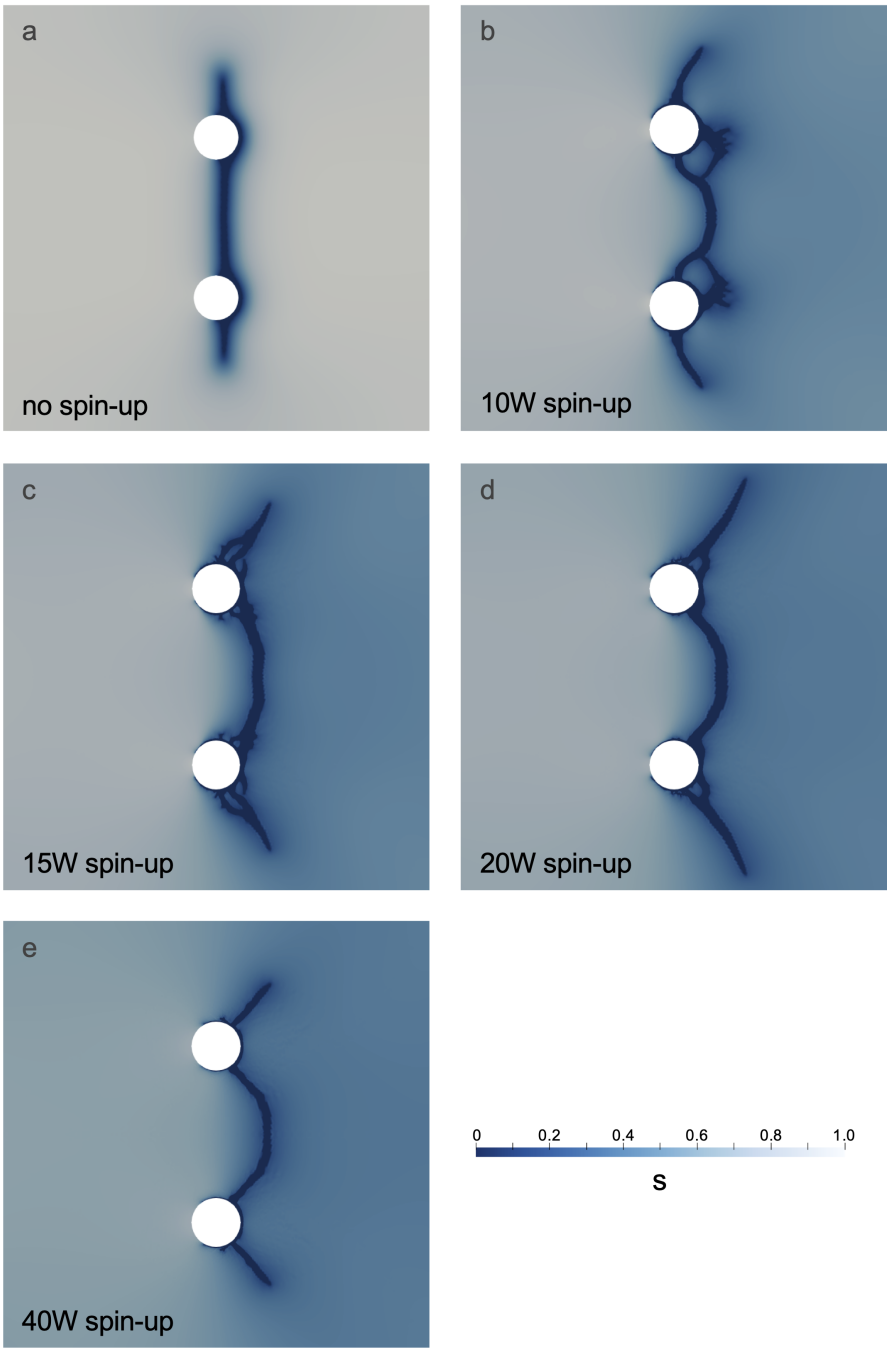

Fig. 5 Phase field of the experiments with ice rises in the center of the ice shelf. (a) no-spin up, (b-e) 10, 15, 20, 40 weeks spin-up respectively.

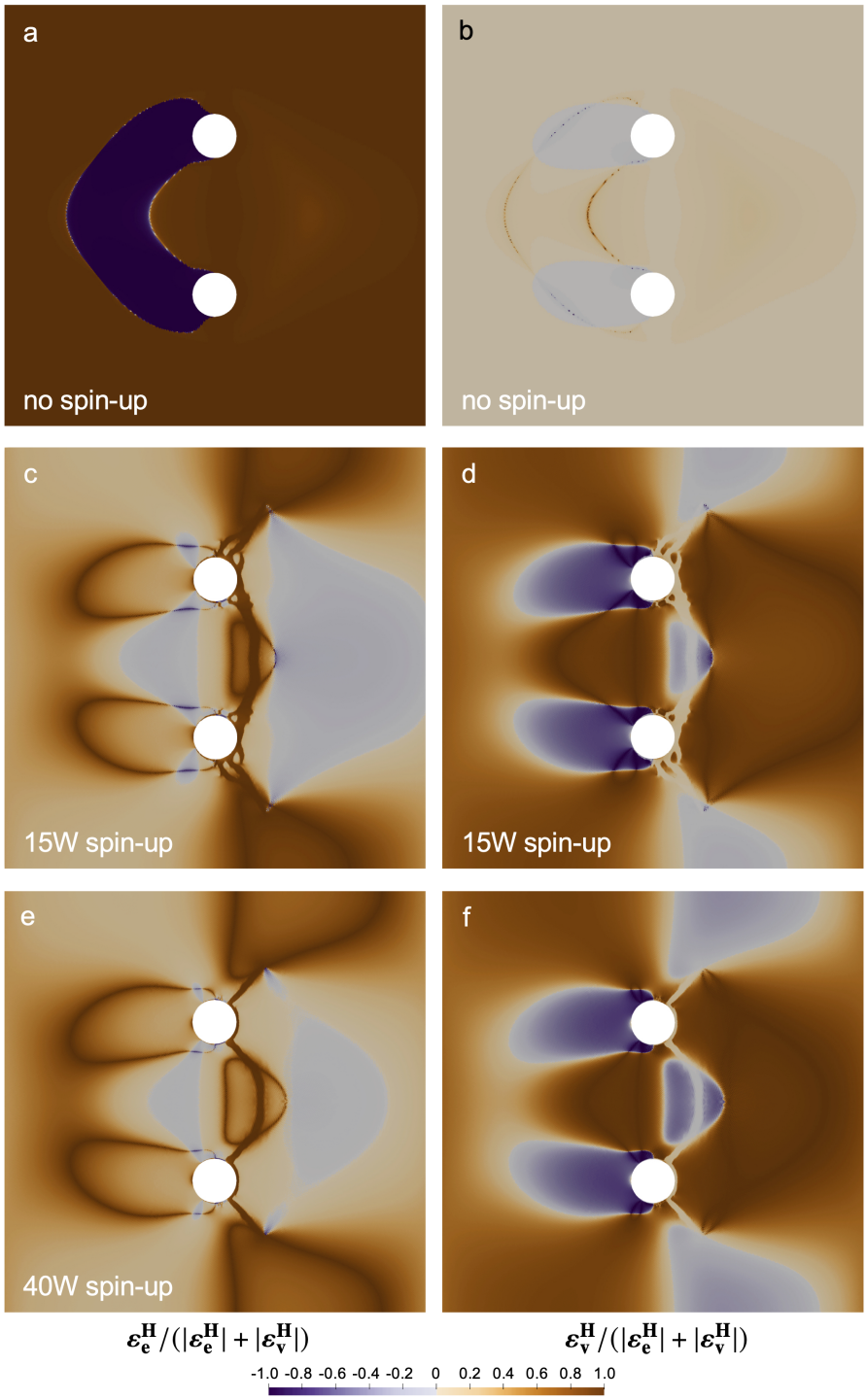

Fig. 6 Hencky strain in x-direction for different experiments. (a,c,e) display $\varepsilon_e^H/(|\varepsilon_e^H| + |\varepsilon_v^H|)$ for no spin-up, 15 and 40 weeks respectively. (b,d,f) display $\varepsilon_v^H/(|\varepsilon_e^H| + |\varepsilon_v^H|)$ for the same situations.

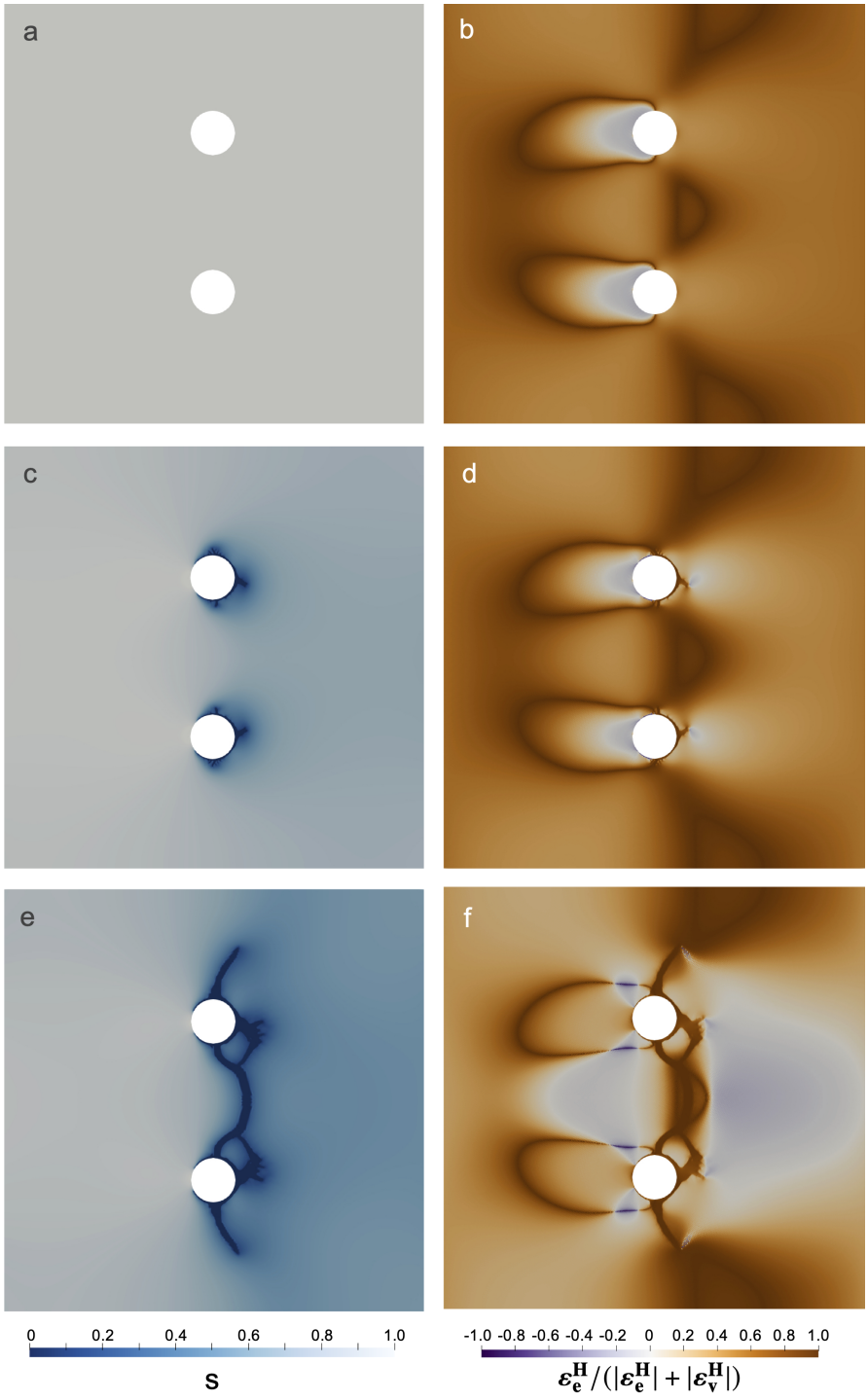

Fig. 7 Temporal evolution of the phase field s in the left panels and the corresponding elastic part of the Hencky strain $\boldsymbol{\varepsilon}_{\mathbf{e}}^{\mathbf{H}}{}_{xx}$ in the right panels for a pre-loading of 10 weeks. The Hencky strain is plotted relative $\boldsymbol{\varepsilon}_{\mathbf{e}}^{\mathbf{H}}/(|\boldsymbol{\varepsilon}_{\mathbf{e}}^{\mathbf{H}}| + |\boldsymbol{\varepsilon}_{\mathbf{v}}^{\mathbf{H}}|)$. Upper row is for $\Delta t = 0$, middle row for $\Delta t = t - t_{SpinUp} = 1.9215 \cdot 10^{-9} s$ and bottom row for $\Delta t = 3.9343 \cdot 10^{-9} s$

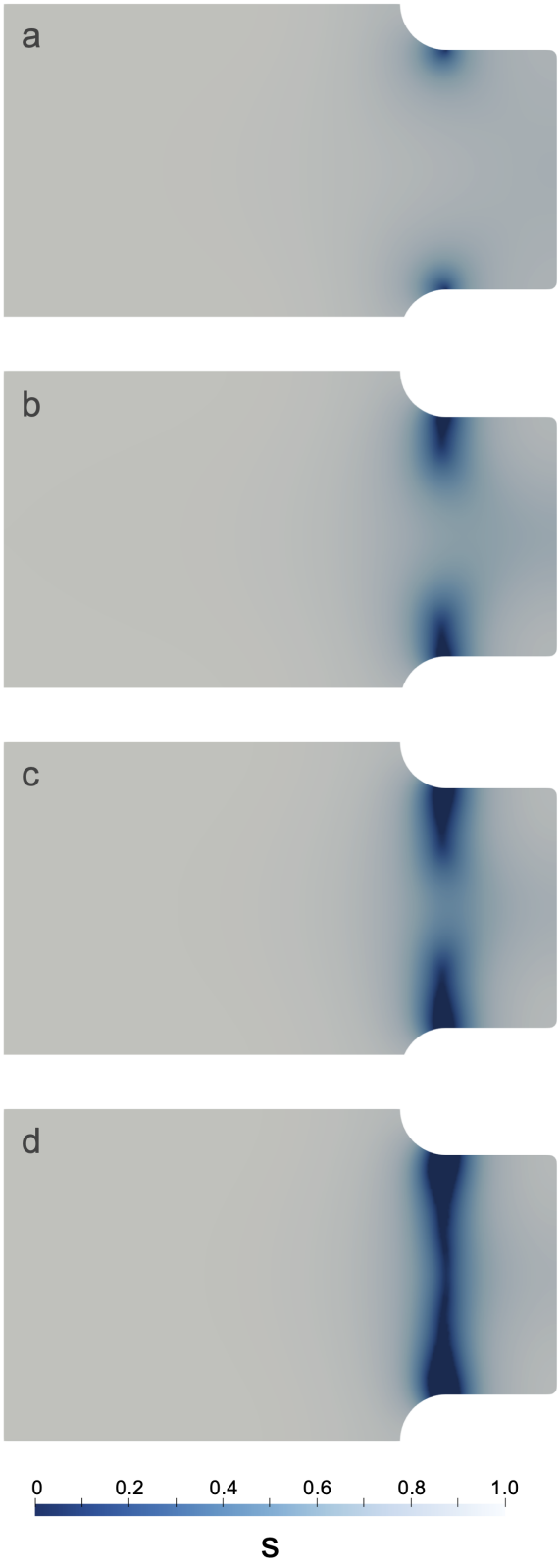

Fig. 8 Temporal evolution of the phase field of the experiments with a floating tongue.
.

4 Released energy estimate based on observations

Satellite and airborne imagery, both optical and radar, can be used to identify cracks in ice. Although this provides only information of the position of the crack at the surface, either via the crack characteristics or additional airborne radar data, an estimate of the vertical dimension can be obtained. We use this to determine the area of the crack faces and to compute the released energy. The satellite imagery we use here is Sentinel 2 (band 2,3,4) in 10 m (medium) resolution. In addition, we use high resolution (0.3 m) optical data (RGB) from the onboard MACS camera system on AWI's polar aircraft. More on the data and its processing is given in [41]. From this imagery we use data along one crack tip to constrain how much energy is released at a typical crack tip. In both cases, we use an energy release rate of $\mathcal{G}_c = 8.071\, J\, m^{-2}$.

The medium resolution is used to measure the individual crack length of all rifts visible in the right panel of Fig. 1. The entire length of all cracks at the surface is 26 387 m. With an ice thickness of 90. . .100 m in this region, an area of 2.4. . .2.6 10^6 m^2 and hence an energy of $\Delta E = 19.2$-21.3 MJ is released during the formation of the cracks.

The high resolution imagery in the right panel of Fig. 9 is used to measure the crack length of each individual crack face. To this end, the length of the crack at the ice shelf surface was determined and the ice thickness based on ice penetrating data was used to compute the newly formed area. The ice thickness is the same as above. The summing up the length of all individual cracks, we find with a total length of 767 m length and energy of 557.1. . .619.0 kJ.

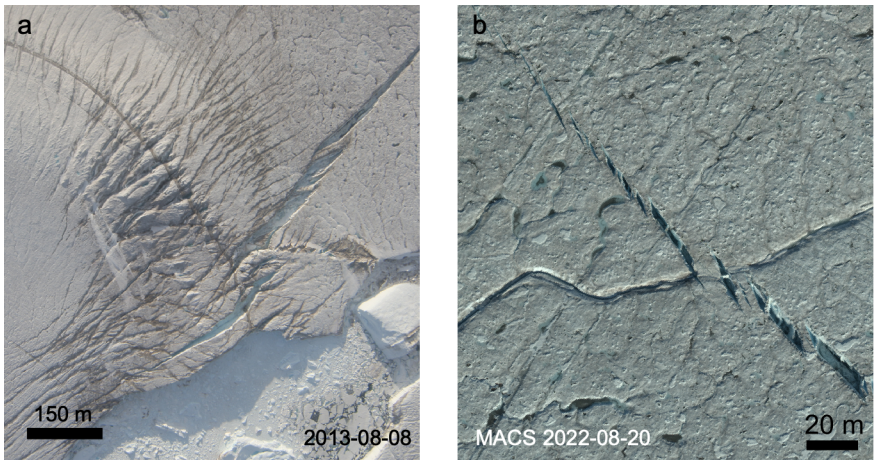

Fig. 9 The left panel displays an image of the onboard Canon camera from 2013-08-08 showing the calving front at the lower ice rise visible in the right panel of Fig. 1. In the right panel a high resolution optical image obtained with the MACS camera system in 30 cm ground resolution of a rift tip is shown.

Comparing to Sentinel-2 imagery in 10 m resolution at the same location and time of Fig. 9b, the crack ends 242 m further in the high resolution MACS imagery than in Sentinel-2 scenes. Next we use the estimated energy of such a rift tip field and add it for each rift in Fig. 1 (right panel). This leads to a total energy of all 15 cracks in this particular calving front situation of 19.2. . .21.3 MJ + 15·(557.1. . .619.0) kJ = 27.6. . .30.6 MJ, which is 44% more released energy than estimated without high resolution imagery.

5 Discussion

In the simulations of Case 1 the crack path is leading to a separation at the downstream side of the ice rises, which is also found in nature. However, at typical calving front situations, the cracks form slightly further upstream than the simulations are showing. The simulated crack propagation in Case 2 is in very good agreement with observations (see Fig. 1 and Fig. 9).

The choice of the boundary condition is affecting the simulation results significantly. Currently, we are fixing the upper and lower boundary at their in vertical direction by choosing a zero displacement condition in vertical direction at those boundaries. This potentially leads to effects at the ice rise margins that are not intended. In future the computational model will be applied to more realistic, and thus irregular, geometries of ice rises. To do so, an extension of the boundary condition along the margin of the ice rise is necessary to prevent penetration, but to similarly allow the ice to disconnect from the grounded ice rises downstream. To this end a no penetration condition as is common in contact mechanics and ice sheet modelling has to be considered. The present investigation represents an extreme case, in which the ice is 'laterally frozen' (kinematically fixed) to the ice rise.

The natural system has a stress boundary condition at the calving front, with water pressure below sea level and traction-free at the ice-atmosphere boundary which was investigated in 2D vertical simulations by [6]. In future, a stress boundary condition along the calving front shall be considered too.

A comparison of the no spin-up simulations of Case 1 and the simulations of Case 2 shows a strong similarity between the crack paths. Both are nearly straight between the ice rises as we expected due to the same boundary conditions. Their are in good agreement with small strain results [30]. Further simulations especially for different spin-up times of Case 2 have to be carried out.

The spin-up runs were conducted to obtain an initial state that represents the stress and strain fields well prior to crack formation. Although this has been a useful method for the problem under consideration, it also caused issues in the transition between spin-up and solving the full problem including the fracture phase field. The pre-loading is so substantial, that the crack formation and propagation sets in nearly instantaneous after the spin-up. This needs further treatment in future, in order to better resemble the natural process. For the situation displayed in Fig. 1 the time between crack formation is about one year. In contrast, in our situation

even after only five weeks of spin-up cracks form instantaneously. It is worth to note, that crack formation in ice shelves is happening extremely fast, with the time scale being narrowed by satellite observations to appear between two subsequent acquisitions, which may in summer be as close as within one day. That the crack propagation within the model is nearly instantaneous is consistent with observations, only the time period between two crack formation events is currently not matching observations.

In our approach a viscoelastic Maxwell material is applied, but we reduced complexity by assuming only an elastic fracture phase field model for crack formation, which can be extended in future to incorporate other crack driving mechanisms. Furthermore, a St. Venant-Kirchhoff material was used primarily for the sake of simplicity. This material law is a widely used, but has issues for large compressive strains. Other material models such as neo-Hooke material formulations can be used as well, leading to a other constitutive relation for the second Piola-Kirchhoff stress tensor $\mathbf{S}$ and consequently to a different evolution equation for the internal variable $\mathbf{C_v}$ [42]. An investigation of the different material models and their influence on the spin-up and fracture phase field are very interesting.

In general, an incorporation of the phase field model of fracture approach into large scale ice sheet models is very favourable, as no adequate formulation of calving is currently incorporated in those models. There are two routes to consider here: (i) to use this approach in a micro-macro coupling, in which at local scale a fracture phase field model is applied. The micro scale fracture phase field model will than be used to derive calving rates, which are incorporated into the level-set method of calving front motion or (ii) to extend the phase field model into an ice sheet wide model with a high resolution mesh in calving front areas and to couple both models directly. In both cases, a velocity formulation of the phase field model for fracture is required, as ice sheet models are in velocity formulation. Both approaches are, however, quite challenging and remain subject of future research.

Comparing the estimate of released energy in medium and high resolution imagery makes evident, that it can only be estimated reliably when using high resolution imagery, as one may underestimate it massively. This highlights the need for high resolution airborne or satellite-borne data for fracture mechanical estimates.

Last but not least, the simulations depend on material parameters that are not well documented and constrained. The basis for $\mathcal{G}_c$ is only K_{Ic} [2], while cracks around the ice rises may also be mode II cracks in some occasion. In addition, the laboratory tests were not conducted for fully consolidated ice, but for very dense firn (experiments: 844.5 to 870.3 kg m^3, consolidated ice: 917 kg m^3). For polycrystalline ice $\mathcal{G}_c$ may thus be smaller than the value used here. Conducting laboratory tests to constrain the material parameters of polycrystalline ice further, would be highly beneficial.

6 Conclusions and future direction

We proposed a viscoelastic phase field method for fracture at finite strains and studied the influence of the loading history on the crack initiation and propagation. The influence of the viscous pre-loading is pronounced and shows the need of a carefully considered spin-ups as glaciers and ice shelves have a long deformation history, which is why large viscous strains occur. Comparison with simulations using small strain reveal that the crack path is similar if no pre-loading is considered, as the crack sets in quite rapidly.

All simulations show crack onset at the downstream side of ice rises. In reality, the downstream side of ice rises is often ice free, which is consistent with our simulations. The crack onset is in observations slightly further upstream, which is likely an effect of the choice of boundary conditions used here.

Ice shows a rate-dependent flow behavior, known by Glen's flow law, which should be incorporated in the future. Also a feedback between the phase field and the viscous deformation is to be evaluated and benchmarked against observations of crack formation.

Since this is the first work of a fracture phase field model for ice considering finite viscoelasticity a lot of open questions regarding the spin-ups and boundary conditions remain. More advanced treatment of the boundary condition is needed to resemble realistic ice shelf situations. Furthermore, a concept to combine large scale ice sheet simulations with fracture phase field simulation needs to be developed in future.

Acknowledgements Airborne data has been acquired with the polar aircrafts of the Alfred-Wegener-Institute Helmholtz Centre of Polar and Marine Research as part of airborne campaigns PRESURV79 (2013) and MACS-NG (2021). R.S. is supported by the German Research Foundation (DFG) under MU 1370/21-1 (501994052). The authors gratefully acknowledge the computing time provided on the high-performance computer Lichtenberg at the NHR Centers NHR4CES at TU Darmstadt. This is funded by the Federal Ministry of Education and Research, and the state governments participating on the basis of the resolutions of the GWK for national high performance computing at universities.

References

1. Petrovic, J.J. *Review Mechanical properties of ice and snow.* Journal of Materials Science 38, 1–6, (2003) https://doi.org/10.1023/A:1021134128038
2. Christmann, J., Müller, R., Webber, K. G., Isaia, D., Schader, F. H., Kipfstuhl, S., Freitag, J., and Humbert, A. *Measurement of the fracture toughness of polycrystalline bubbly ice from an Antarctic ice core.* Earth Syst. Sci. Data, 7, 87–92, (2015) https://doi.org/10.5194/essd-7-87-2015
3. Reeh, N., Christensen, E., Mayer, C., and Olesen, O. *Tidal bending of glaciers: A linear viscoelastic approach.* Annals of Glaciology, 37, 83-89. (2003) doi:10.3189/172756403781815663

4. Gudmundsson, G. H. *Ice-stream response to ocean tides and the form of the basal sliding law.* The Cryosphere, 5, 259–270, (2011) https://doi.org/10.5194/tc-5-259-2011
5. Christmann, J., Helm, V., Kahn, S. A., Kleiner, T., Müller, R., Morlighem, M., Neckel, N., Rückamp, M., Steinhage, D., Zeising, O., and Humbert, A. *Elastic defor- mation plays a non-negligible role in Greenland's outlet glacier flow.* Nature Communications Earth & Environment, (2021) https://doi.org/10.1038/s43247-021-00296-3
6. Christmann J, Müller R, Humbert A *On nonlinear strain theory for a viscoelastic material model and its implications for calving of ice shelves.* Journal of Glaciology 95(250):212–224, (2019).
7. Humbert, A., Christmann, J., Corr, H. F. J., Helm, V., Höyns, L.-S., Hofstede, C., Müller, R., Neckel, N., Nicholls, K. W., Schultz, T., Steinhage, D., Wolovick, M., and Zeising, O. *On the evolution of an ice shelf melt channel at the base of Filchner Ice Shelf, from observations and viscoelastic modeling.*, The Cryosphere, 16, 4107–4139, (2022) https://doi.org/10.5194/tc-16-4107-2022
8. Francfort, G. A., and Marigo, J. J. *Revisiting brittle fracture as an enerty minimization problem.* Journal of the Mechanics and Physics of Solids, 46(8), pp. 1319–1342, (1998).
9. Bourdin, B., Francfort, G. A., and Marigo, J. J. *Numerical experiments in revisited brittle fracture.* Journal of the Mechanics and Physics of Solids, 48(4), pp. 797–826, (2000).
10. Bourdin, B. *Numerical implementation of the variational formulation for quasi-static brittle fracture.* Interfaces and Free Boundaries, 9(3), pp. 411–430, (2007).
11. Borden, M. J., Verhoosel, C. V., Scott, M. A. Hughes, T. J., and Landis, C. M. *A phase-field description of dynamic brittle failure.* Computer Methods in Applied Mechanics and Engineering, 217, pp. 77–95, (2012).
12. Schlüter, A., Kuhn, C., Müller, R., and Gross, D. *An investigation of intersonic fracture using a phase field model.* Archive of Applied Mechanics, 86, pp. 321–333, (2016).
13. Ren, H. L., Zhuang, X. Y., Anitescu, C., and Rabczuk, T. *An explicit phase field method for brittle dynamic fracture.* Computers & Structures, 217, pp. 45–56, (2019).
14. Lo, Y. S., Borden, M. J., Ravi-Chandar, K., and Landis, C. M. *A phase-field model for fatigue crack growth.* Journal of the Mechanics and Physics of Solids, 132, p. 103684, (2019).
15. Schreiber, Ch., Kuhn, Ch., Müller, R., and Zohdi, T. *A phase field Modeling approach of cyclic fatigue crack growth.* International Journal of Fracture, 225, pp. 89–100, (2020).
16. Yan, S., Schreiber, C., and Müller, R. *An efficient implementation of a phase field model for fatigue crack growth.* International Journal of Fracture, pp. 1–14, (2022).
17. Heider, Y. *A review on phase-field modeling of hydraulic fracturing.* Engineering Fracture Mechanics, 253, pp. 1–24, (2021).
18. Aldakheel, F., Noii, N., Wick, T. and Wriggers, P. *A global–local approach for hydraulic phase-field fracture in poroelastic media.* Computers & Mathematics with Applications, 91, pp. 99–121, (2021).
19. Teichtmeister, S., Kienle, D., Aldakheel, F., and Keip, M. A. *Phase field modeling of fracture in anisotropic brittle solids.* International Journal of Non-Linear Mechanics, 97, pp. 1–21, (2017).
20. Bleyer, J. and Alessi, R. *Phase-field modeling of anisotropic brittle fracture including several damage mechanisms.* Computer Methods in Applied Mechanics and Engineering, 336, pp. 213–236, (2018).
21. Schreiber, C. *Phase Field Modeling of Fracture: Fatigue and Anisotropic Fracture Resistance.* Ph.D. Thesis, TU Kaiserslautern, (2021).
22. Ambati, M., Gerasimov, T., and De Lorenzis, L. *Phase-field modeling of ductile fracture.* Computational Mechanics, 55(5), pp. 1017–1040, (2015).
23. Miehe, C., Aldakheel, F., and Raina, A. *Phase field modeling of ductile fracture at finite strains: A variational gradient-extended plasticity-damage theory.* International Journal of Plasticity, 84, pp. 1–32, (2016).
24. Noll, T., Kuhn, Ch., Olesch, D., and Müller, R. *3D phase field simulations of ductile fracture.* GAMM Mitteilungen, 43, (2020).

25. Shen, R., Waisman, H., and Guo, L. *Fracture of viscoelastic solids modeled with a modified phase field method.* Computer Methods in Applied Mechanics and Engineering, 346, pp. 862–890, (2019).
26. Yin, B., and Kaliske, M. *Fracture simulation of viscoelastic polymers by the phase-field method.* Computational Mechanics, 65, 293-309, (2020).
27. Dammaß, F., Ambati, M., and Kästner, M., *A unified phase-field model of fracture in viscoelastic materials.* Continuum Mechanics and Thermodynamics, 1-23, (2021).
28. Sun, X., and Ravindra D. *A poro-damage phase field model for hydrofracturing of glacier crevasses.* Extreme Mechanics Letters 45:101277, (2021).
29. Clayton, T., Duddu, R., Siegert, M. and Martínez-Pañeda, E. *A stress-based poro-damage phase field model for hydrofracturing of creeping glaciers and ice shelves.* Engineering Fracture Mechanics, 272, pp. 1–24, (2022).
30. Sondershaus, R., Humbert, A., Müller, R. *A phase field model for fractures in ice shelves.* PAMM, 2023, 22. Jg., Nr. 1, S. e202200256.
31. Lee E H *Elastic-Plastic Deformation at Finite Strains.* Journal of Applied Mechanics 36(1):1–6, (1969).
32. Haupt, P. *Continuum Mechanics and Theory of Materials.* Springer Berlin, Heidelberg, (2000).
33. Becker, W. and Gross, D. *Mechanik elastischer Körper und Strukturen.* Berlin, Heidelberg, s.l., Springer Berlin Heidelberg, (2002), https://dx.doi.org/10.1007/978-3-642-56124-5
34. Neff, P., Ghiba, ID. and Lankeit, J. *The Exponentiated Hencky-Logarithmic Strain Energy. Part I: Constitutive Issues and Rank-One Convexity*. J Elast 121, 143–234, (2015) https://doi.org/10.1007/s10659-015-9524-7
35. Ambrosio, L. and Tortorelli, V.M. *Approximation of Functional Depending on Jumps by Elliptic Functional via t-Convergence*. Communications on Pure and Applied Mathematics 43 (8): 999–1036, (1990).
36. B. Bourdin *Une Méthode variationnelle en mécanique de la rupture.* PhD thesis, Université Paris-Nord, (1998).
37. A. Chambolle *An approximation result for special functions with bounded deformation.* J. Math. Pure Appl., 83(7):929–954, (2004).
38. Alnaes, M. S., Blechta, J., Hake, J., Johansson, A., Kehlet, B., Logg, A., Richardson, C., Ring, J., Rognes, M. E. and Wells, G. N. *The FEniCS Project Version 1.5.* Archive of Numerical Software 3, (2015).
39. Amestoy, P.R., Duff, I.S., Koster, J., L'Excellent, J.-Y. *A Fully Asynchronous Multifrontal Solver Using Distributed Dynamic Scheduling.* SIAM Journal on Matrix Analysis and Applications, 23 (1), 15-41, (2001)
40. Geuzaine, C., and Remacle, J.-F. *Gmsh: a three-dimensional finite element mesh generator with built-in pre- and post-processing facilities.* International Journal for Numerical Methods in Engineering 79 (11), pp. 1309-1331, (2009).
41. Humbert, A., Helm, V., Neckel, N., Zeising, O., Rückamp, M., Khan, S. A., Loebel, E., Gross, D., Sondershaus, R., and Müller, R. *Precursor of disintegration of Greenland's largest floating ice tongue.* The Cryosphere Discuss. (2022), [preprint], https://doi.org/10.5194/tc-2022-171, in review
42. Christmann J. *Viscoelastic Modeling of Calving Processes at Antarctic Ice Shelves.* Ph.D. Thesis, TU Kaiserslautern, (2017).